Black Box-Based Incremental Reduced-Order Modeling Framework of Inverter-Based Power Systems

WEIHUA ZHOU [1,2] (Member, IEEE), AND JEF BEERTEN [1,2] (Senior Member, IEEE)

[1]Department of Electrical Engineering, KU Leuven, 3000 Leuven, Belgium
[2]EnergyVille, 3600 Genk, Belgium

CORRESPONDING AUTHOR: WEIHUA ZHOU (e-mail: weihua.zhou@ieee.org).

ABSTRACT Due to the capability to perform participation factor analysis and oscillation origin location, the state–space model (SSM)-based eigenvalue method has been widely used for stability assessment of inverter-penetrated power systems. However, possible internal confidentiality of inverters impedes the derivation of their SSMs. In addition, conventional derivation procedure of system SSM can be tedious when complicated transmission network topology and various transmission cables are involved, which may result in a high-order system SSM. To this end, this article presents a black box-based incremental reduced-order modeling framework. The reduced-order SSMs of the inverters and transmission cables are extracted from their dq-domain admittance frequency responses and abc-domain impedance frequency responses, respectively, by the matrix fitting algorithm. Then, the SSM operators proposed in this article recursively assemble the components' fitted SSMs in the similar manner as the impedance model operator-based recursive components' impedance aggregation, while preserving the dynamics of individual components. Simulation results show that the presented state–space modeling framework can properly identify the state–space models of black-box devices at component modeling stage, simplify assembling procedure at subsystems/components integration stage, and release computational burden at system participation factor analysis stage.

INDEX TERMS Black box, inverter, matrix fitting, order reduction, state–space model (SSM) operator, transmission cable.

NOMENCLATURE

Abbreviations

AFR	Admittance frequency response.
CCM	Component connection method.
FOM	Full-order model.
IFR	Impedance frequency response.
IMO	Impedance model operator.
IMPO	Impedance model parallel operator.
IMSO	Impedance model series operator.
PCC	Point of common coupling.
PF	Participation factor.
ROM	Reduced-order model.
SSM	State–space model.
SSMO	State–space model operator.
SSMPO	State–space model parallel operator.
SSMSO	State–space model series operator.
VF/MF	Vector/matrix fitting.
VSC	Voltage source converter.

I. INTRODUCTION

Renewable energies, such as wind power and solar power, have increasingly been penetrating into the conventional synchronous generator-dominated power systems in recent years [1]. Solid-state voltage source converters (VSCs) are widely employed as the interface between these renewable energies and the utility grid [2]. However, wideband instability phenomena may occur due to undesirable interactions between the multiple-timescale control loops of the VSCs and weak grids, which may threaten the safe and reliable operation of the VSC-based power systems [3].

The state–space model (SSM)-based eigenvalue method can draw a global picture of the system modes, based on which the dynamic contributions of each state variable to these modes can be calculated by the participation factor (PF) analysis, and the problematic device can further be identified [4]. Thanks to these advantages, the eigenvalue method has been widely applied to analyze the stability of the VSC-based power systems [4], [5], [6], [7], [8]. In [4], [5], the power system as a whole is modeled as a high-dimensional SSM, which does not take advantage of the interconnection relationship among individual components. Therefore, the conventional state-space modeling method risks a lack of simplicity, modularity, and scalability for VSC-based power systems with complicated transmission network. To this end, the time-domain component connection method (CCM) was initially presented in [6]. Individual components/subsystems are identified from the whole power system and modeled independently, based on which the composite system model is derived by combining these small SSMs according to their interconnection relationship that can be described as a sparse linear algebra matrix. The time-domain CCM was later developed for state–space modeling at converter level in [7], [8], [9] and at system level in [10]. The combination of simplicity, modularity, and scalability with the advantage of matrix algebra and sparsity in the time-domain CCM makes it more suitable for large-scale VSC-based power systems [6].

However, the popularization of the time-domain CCM is impeded by the black-boxed feature of internal structure and parameters of individual components [11]. Based on analytical/measured impedance/admittance models of individual components, this black-box issue has been dealt with by various modified CCMs [12], [13], [14], [15], [16]. Frequency-domain CCM is presented in [12], [13], [14], where one subsystem composed of all VSCs and the other subsystem composed of the connection network are identified from the whole power system and characterized as two diagonal transfer function matrices. The two matrices are then assembled as a feedback control system, the open-loop transfer function matrix of which is used to predict the system's global stability. Similar to the aforementioned time-domain CCM, the impacts of each component on global stability and dynamic interactions among individual components can also be emphasized using the frequency-domain CCM. However, if the two-dimensional dq-domain impedance models are adopted, the order of the open-loop transfer function matrix can be twice as the number of the VSCs, which may be tedious and bring in heavy computational burdens for eigenvalues or determinant calculation of the high-dimensional matrix [12], [14].

An impedance model is the transfer function equivalence of an SSM, if the input and output variables of the SSM are input current signal and terminal voltage signal, respectively [11]. Based on this inherent relationship, the vector/matrix fitting (VF/MF) algorithm initially proposed in [17], [18] is employed in [15] at converter level, in [16] at subsystem level, and in [11], [19] at system level to extract the SSMs composed of virtual state variables from a set of admittance frequency responses (AFRs) or impedance frequency responses (IFRs). The extracted converters' SSMs in [15] or subsystems' SSMs in [16] are then combined based on the time-domain CCM for eigenvalue analysis, whereas the extracted system's SSMs in [11], [19] are directly used for eigenvalue analysis. Due to the preprocessed components impedance aggregation, the structure of the interconnection matrix in [16] is clearly simpler than that in [15] at the cost of converter-level PF analysis. Exceptionally, no interconnection matrix derivation is required for [11], [19], and the converter-level PF analysis is thus impossible. The impedance model operators (IMOs) in the incremental impedance aggregation, i.e., impedance series and parallel operators, are clearly more modular, more scalable, and simpler than the interconnection matrix in the time-domain CCM. Therefore, similar incremental series and parallel operators that are defined as the state–space model operators (SSMOs) in this article instead of the interconnection matrix are desired for the time-domain CCM in order to combine the advantages of the IMOs and the converter-level PF analysis.

Although the aforementioned modified CCMs in [12], [13], [14], [15], [16], when compared to the conventional state–space modeling method, can partly solve the black-box issue at converter-level modeling stage and the nonmodularity/unscalability issue at subsystem-level assembling/aggregation stage, the order of the derived system SSM can still be very high when parasitic capacitance and frequency-dependent resistance and inductance of transmission cables are considered [20], [21], [22], [23]. Various white box-based model order reduction techniques, e.g., neglecting the inner-loop dynamics [24], the singular perturbations technique [25], and the PF analysis method [4], have been adopted to ease the computational burdens while preserving the stability characteristic in the frequency range of interest, e.g., low-frequency modes [24], [25] or the medium and high-frequency modes [4]. Differently, the VF/MF algorithm can be regarded as a black box-based model order reduction technique, since it preferentially captures the dominant magnitude resonance peaks of the Bode plot [26].

In order to fill in the aforementioned research gaps, a black box-based incremental reduced-order modeling framework of the VSC- and transmission cable-based power systems is presented in this article. The reduced-order SSMs of VSCs and transmission cables are extracted from the dq-domain AFRs and abc-domain IFRs, respectively, by the MF algorithm. Then, the SSMOs proposed in this article recursively assemble the components' fitted SSMs in the similar manner as the IMO-based recursive components' impedance aggregation, while preserving the dynamics of individual components.

The main contributions of this article can be summarized as follows.

1) A black box-based frequency range-oriented reduced-order models (ROMs) of VSCs and transmission cables are presented.
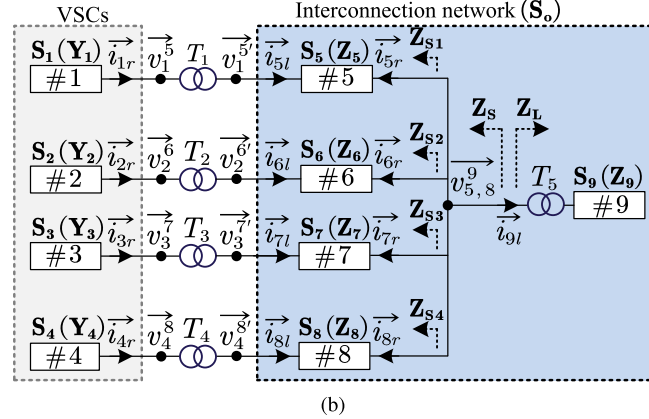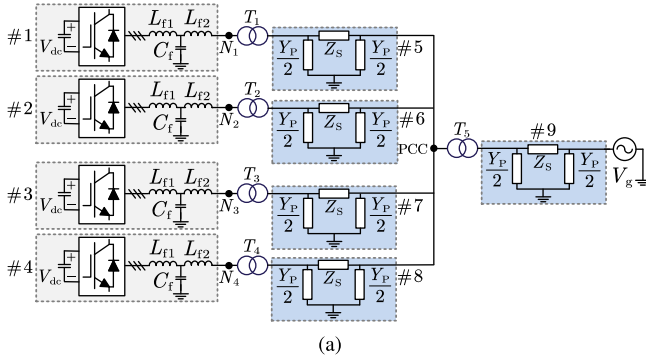2) The SSMOs are proposed to incrementally integrate components'/subsystems' SSMs.

FIGURE 1. System model of a typical inverter-based power system. (a) Circuit model. (b) Equivalent dq-domain state–space (admittance/impedance) network model.

FIGURE 2. Time-domain CCM-based interconnection relationship among different components/subsystems in Fig. 1(b).

3) An IFR/AFR-based oscillation origin location method is developed.

4) A modular systematic state–space modeling framework is constructed, which includes converter-level IFR-based state–space modeling, subsystem-level SSMO-based components assembling, and system-level virtual state variable-based PF analysis.

The rest of this article is organized as follows. In Section II, the theoretical basis is reviewed. The principle of the proposed modeling framework is explained in Section III. In Section IV, its implementation procedure is shown. The PF analysis and time-domain verification are shown in Section V. Finally, Section VI concludes this article.

II. THEORETICAL BASIS

In this section, the topology of the inverter-based power system under study is described, followed by the introduction of the time-domain CCM and the IMOs.

A. SYSTEM DESCRIPTION

Four LCL-filtered VSCs in Fig. 1(a) are connected with the utility grid through a radial transmission network composed of five cables that are represented as single-Π distributed-parameter circuit models and five step-up transformers. The internal control structures and parameters of the four VSCs
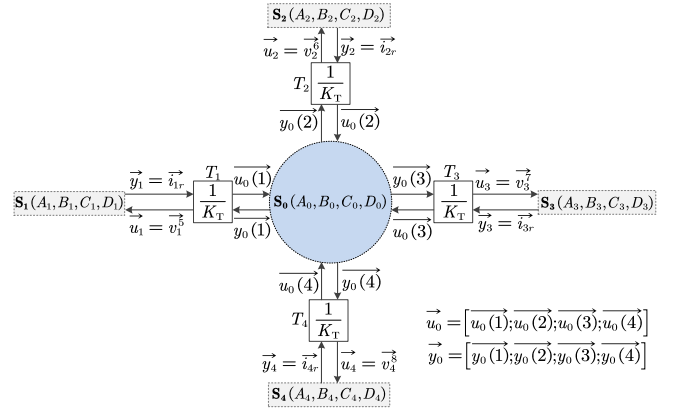
are assumed to be unknown. In Fig. 1(b), the four VSCs and five cables are represented as the dq-domain SSMs (admittance/impedance models), shown as $\mathbf{S_1}$-$\mathbf{S_4}$ ($\mathbf{Y_1}$-$\mathbf{Y_4}$) and $\mathbf{S_5}$-$\mathbf{S_9}$ ($\mathbf{Z_5}$-$\mathbf{Z_9}$), respectively. The dq-domain state–space and admittance/impedance representations of individual components provide the basis for further time-domain CCM and frequency-domain admittance/impedance aggregation, respectively.

B. TIME-DOMAIN CCM

Fig. 2 shows the time-domain CCM-based interconnection relationship among different components/subsystems in Fig. 1(b), where $\mathbf{S_0}$ and $\mathbf{S_1}$-$\mathbf{S_4}$ model the interconnection network and the four VSCs, respectively. K_T is the transformer ratio of T_1-T_4. Specifically, $\mathbf{S_0}$-$\mathbf{S_4}$ can be represented as

$$\Delta \dot{\overrightarrow{x_i}} = A_i \Delta \overrightarrow{x_i} + B_i \Delta \overrightarrow{u_i}, \quad \Delta \overrightarrow{y_i} = C_i \Delta \overrightarrow{x_i} + D_i \Delta \overrightarrow{u_i} \quad (1)$$

where $\overrightarrow{x_i}$, $\overrightarrow{u_i}$, and $\overrightarrow{y_i}$ ($i \in [0, 4]$) denote the vectors of state, input, and output variables of the ith component/subsystem, respectively. In addition, the symbol Δ denotes the small-signal perturbation.

Then, the overall system model that ignores the interconnection relationship can be derived by diagonally stacking the matrices of (1), shown as

$$\Delta \dot{\overrightarrow{x_{stac}}} = A_{stac} \Delta \overrightarrow{x_{stac}} + B_{stac} \Delta \overrightarrow{u_{stac}}$$
$$\Delta \overrightarrow{y_{stac}} = C_{stac} \Delta \overrightarrow{x_{stac}} + D_{stac} \Delta \overrightarrow{u_{stac}} \quad (2)$$

where $\overrightarrow{x_{stac}} = [\overrightarrow{x_0}; ...\overrightarrow{x_2}; ...\overrightarrow{x_4}]$, $\overrightarrow{u_{stac}} = [\overrightarrow{u_0}; ...\overrightarrow{u_2}; ...\overrightarrow{u_4}]$, and $\overrightarrow{y_{stac}} = [\overrightarrow{y_0}; ...\overrightarrow{y_2}; ...\overrightarrow{y_4}]$ are the stacked vectors of state, input, and output variables of all components/subsystems, respectively. In addition, $A_{stac} = \text{diag}(A_0, ...A_2, ...A_4)$, $B_{stac} = \text{diag}(B_0, ...B_2, ...B_4)$, $C_{stac} = \text{diag}(C_0, ...C_2, ...C_4)$, and $D_{stac} = \text{diag}(D_0, ...D_2, ...D_4)$ are the stacked block diagonal matrices.

Next, assume that the vectors of system input variables $\overrightarrow{u_{sys}}$ and system output variables $\overrightarrow{y_{sys}}$ are $\overrightarrow{i_{1r}}$ and $\overrightarrow{v_1^5}$, respectively. By further considering the interconnection relationship
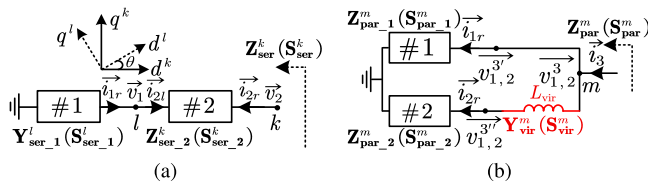
FIGURE 3. Two basic components/subsystems connection cases. (a) Series connection. (b) Parallel connection.

in Fig. 2, equation (2) can be modified in order to eliminate some input variables in $\overrightarrow{u_{\text{stac}}}$ that do not belong to $\overrightarrow{u_{\text{sys}}}$ and some output variables in $\overrightarrow{y_{\text{stac}}}$ that do not belong to $\overrightarrow{y_{\text{sys}}}$ by

$$\Delta \overrightarrow{u_{\text{stac}}} = R_1 \Delta \overrightarrow{y_{\text{stac}}} + R_2 \Delta \overrightarrow{u_{\text{sys}}}$$
$$\Delta \overrightarrow{y_{\text{sys}}} = R_3 \Delta \overrightarrow{y_{\text{stac}}} + R_4 \Delta \overrightarrow{u_{\text{sys}}} \qquad (3)$$

from which R_1-R_4 can be calculated accordingly.

Finally, the system SSM can be derived by substituting (3) into (2), shown as

$$\Delta \overrightarrow{\dot{x}_{\text{sys}}} = \Delta \overrightarrow{\dot{x}_{\text{stac}}} = A_{\text{sys}} \Delta \overrightarrow{x_{\text{sys}}} + B_{\text{sys}} \Delta \overrightarrow{u_{\text{sys}}}$$
$$\Delta \overrightarrow{y_{\text{sys}}} = C_{\text{sys}} \Delta \overrightarrow{x_{\text{sys}}} + D_{\text{sys}} \Delta \overrightarrow{u_{\text{sys}}} \qquad (4)$$

where

$$A_{\text{sys}} = A_{\text{stac}} + B_{\text{stac}} R_1 (I - D_{\text{stac}} R_1)^{-1} C_{\text{stac}}$$
$$B_{\text{sys}} = B_{\text{stac}} R_1 (I - D_{\text{stac}} R_1)^{-1} D_{\text{stac}} R_2 + B_{\text{stac}} R_2$$
$$C_{\text{sys}} = R_3 (I - D_{\text{stac}} R_1)^{-1} C_{\text{stac}}$$
$$D_{\text{sys}} = R_3 (I - D_{\text{stac}} R_1)^{-1} D_{\text{stac}} R_2 + R_4. \qquad (5)$$

The modular state–space modeling of individual components/subsystems makes the time-domain CCM much scalable. In addition, thanks to the sparsity of the diagonal matrices in (5), computational burden of A_{sys} can be released to some extent. Even so, R_1-R_4 can still have high dimensions if the number of the interconnection nodes is high. They also should be derived repeatedly once the system topology undergoes any slight modification. In addition, although R_1-R_4 can be derived based on only components/subsystems input and output variables, as shown in (3), the conventional time-domain CCM cannot theoretically derive A_{stac}, B_{stac}, C_{stac}, and D_{stac} if internal structure and parameters of individual components/subsystems are unknown.

C. IMPEDANCE MODEL OPERATORS

Two basic interconnection relationships, i.e., series connection and parallel connection, between two independent components/subsystems are illustrated in Fig. 3. Before the impedance aggregation, the two dq-domain admittance/impedance models established in their local reference frames should be reformulated in a unified global reference frame [27]. Take Fig. 3(a) as an example, $\mathbf{Y}^l_{\text{ser\_1}}$ is rotated from the l-node reference frame to the k-node reference frame, based on which the total series impedance $\mathbf{Z}^k_{\text{ser}}$ is

calculated as

$$\mathbf{Z}^k_{\text{ser}} = \text{inv}(\mathbf{Y}^k_{\text{ser\_1}}) + \mathbf{Z}^k_{\text{ser\_2}}$$
$$= \mathbf{R}(\theta)\text{inv}(\mathbf{Y}^l_{\text{ser\_1}})\mathbf{R}^{-1}(\theta) + \mathbf{Z}^k_{\text{ser\_2}}$$
$$= \mathbf{Y}^l_{\text{ser\_1}} \oplus' \mathbf{Z}^k_{\text{ser\_2}} \qquad (6)$$

where the superscripts l and k denote the reference frames where the dq-domain admittance/impedance models are derived. $\mathbf{R}(\theta) = [\cos\theta, \sin\theta; -\sin\theta, \cos\theta]$ is the rotation matrix, and θ is the angle difference between the l-node and k-node reference frames. In addition, the impedance model series operator (IMSO) is defined as $\oplus'$ in (6).

Unlike the series connection case, no dq-domain impedance matrix rotation is required for the parallel connection case shown in Fig. 3(b), since the two subsystems are connected to the same node m, thus having the same local reference frame defined by the voltage vector at node m. The total parallel impedance $\mathbf{Z}^m_{\text{par}}$ is calculated as

$$\mathbf{Z}^m_{\text{par}} = \frac{\mathbf{Z}^m_{\text{par\_1}} \mathbf{Z}^m_{\text{par\_2}}}{\mathbf{Z}^m_{\text{par\_1}} + \mathbf{Z}^m_{\text{par\_2}}} = \mathbf{Z}^m_{\text{par\_1}} \odot' \mathbf{Z}^m_{\text{par\_2}} \qquad (7)$$

where the superscript m denotes the reference frame where the dq-domain impedance models are derived. In addition, the impedance model parallel operator (IMPO) is defined as $\odot'$ in (7). Note that the zero-valued virtual inductance L_{vir} is designed for the SSM integration, and thus not considered here for the impedance model aggregation.

Compared to the aforementioned time-domain CCM, the IMSO and IMPO are clearly more modular and scalable, which can be employed recursively to derive the aggregated dq-domain impedance matrix of Fig. 1(b). However, components' dynamics are merged in the aggregated impedance model, and oscillation origin can thus not be located. A key motivation for the proposed SSMOs is to merge the benefits of the time-domain CCM and IMOs. Specifically, the system SSM is formulated similarly to the aggregated impedance model built using the IMOs, but it still retains the dynamics of the components.

III. PROPOSED BLACK BOX-BASED INCREMENTAL REDUCED-ORDER MODELING FRAMEWORK
In this section, the reduced-order modeling method of the VSCs and cables is presented, followed by the introductions of the proposed SSMOs and state–space modeling framework.

A. PROPOSED BLACK BOX-BASED REDUCED-ORDER MODELING METHOD
The proposed black box-based reduced-order modeling method of the VSCs and cables consists of two main steps. In step 1, the dq-domain AFRs of VSCs and abc-domain IFRs of cables, e.g., $f(\omega_1)$, $f(\omega_2)$, ..., $f(\omega_P)$, are obtained, where P is the number of the sample frequencies. In step 2, the AFRs/IFRs obtained in step 1 are employed to determine the minimum orders for both the VSCs and cables in order to achieve the tradeoff between simplicity and accuracy. The

full order of a VSC is normally lower than 20th, e.g., the full order of a VSC with current control inner loop, PLL, dc-link voltage control, and ac voltage magnitude control is 17th [9]. The minimum orders of the VSCs are thus determined in a trial-and-error way using the MF algorithm, i.e., the fitting order is gradually increased from 2nd until the fitting error is satisfied. The fitted transfer function matrix is in the form of

$$f_{\text{MF}}(s) = \frac{R_m}{s - P_m} + \frac{R_{m-1}}{s - P_{m-1}} ... + \frac{R_1}{s - P_1} + D_{\text{MF}}$$
$$= C_{\text{MF}}(sI_{mk \times mk} - A_{\text{MF}})^{-1}B_{\text{MF}} + D_{\text{MF}} \quad (8)$$

where $A_{\text{MF}} = \text{diag}(\text{diag}(P_1, P_2...P_m),..., \text{diag}(P_1, P_2...P_m))_k$, $B_{\text{MF}} = \text{diag}(I_{m \times 1}, ..., I_{m \times 1})_k$, and $C_{\text{MF}} = [R_1(:, 1), R_2(:, 1)..., R_m(:, 1), R_1(:, 2), R_2(:, 2)..., R_m(:, 2), ..., R_1(:, k), R_2(:, k)..., R_m(:, k)]$. In addition, D_{MF} is the $k \times k$ matrix. The fitting error of the generated m th-order transfer function matrix is defined as

$$E(f_{\text{MF}}(s))|_{s=j\omega} = \sqrt{\sum_{k=1}^{P} (f_{\text{MF}}(\omega_k) - f(\omega_k))^2/P}. \quad (9)$$

Since various control loops may make the VSCs nonpassive in certain frequency ranges, e.g., current control loop-related high-frequency nonpassivity and PLL-related low-frequency nonpassivity, stability/passivity enforcement in the MF algorithm should be disabled for the VSCs. Otherwise, the identification of the right-half-plane poles may fail.

Unlike the VSCs, the minimum order of the multiple-Π lumped-parameter RLC circuit model for a 800 km long cable can be 600th in order to reproduce the frequency-dependent electrical characteristics up to 5 kHz [23]. Since one magnitude peak of the Bode diagram of the IFRs can be captured by order 2nd when using the MF algorithm, the minimum order of a cable can be only about twice as the number of the magnitude peaks located in the frequency range of interest in order to reproduce all of the eigenvalues of interest. The proposed MF algorithm-based state–space modeling method is thus a model order reduction method. The minimum orders of the cables are also determined in a trial-and-error way by gradually increasing the fitting order from twice the number of the magnitude peaks to be captured until the fitting error curve is smooth. Since the impedance of the transmission cables is passive in all frequency ranges, stability/passivity enforcement in the MF algorithm should be enabled for the cables. Based on the fitted abc-domain SSM of the cables, the corresponding dq-domain SSM of the cables can be further derived.

B. PROPOSED INCREMENTAL STATE–SPACE MODELING METHOD

1) PROPOSED STATE–SPACE MODEL SERIES OPERATOR (SSMSO) $\oplus$

Similar to the dq-domain admittance/impedance matrices aggregation in Fig. 3(a), the SSMs of components/subsystems #1 and #2 developed in their local reference frames should also be reformulated in a unified global reference frame. The

SSMs of component/subsystem #1 in the l-node and k-node reference frames, i.e., $\mathbf{S}^l_{\text{ser}\_1}$ and $\mathbf{S}^k_{\text{ser}\_1}$, are assumed as

$$\Delta \overset{\bullet}{\overrightarrow{x^l_{\text{ser}\_1}}} = A^l_{\text{ser}\_1} \Delta \overrightarrow{x^l_{\text{ser}\_1}} + B^l_{\text{ser}\_1} \left[\Delta v^l_{1d}, \Delta v^l_{1q} \right]^T$$
$$\left[\Delta i^l_{1rd}, \Delta i^l_{1rq} \right]^T = C^l_{\text{ser}\_1} \Delta \overrightarrow{x^l_{\text{ser}\_1}} + D^l_{\text{ser}\_1} \left[\Delta v^l_{1d}, \Delta v^l_{1q} \right]^T$$
(10)

and

$$\Delta \overset{\bullet}{\overrightarrow{x^k_{\text{ser}\_1}}} = A^k_{\text{ser}\_1} \Delta \overrightarrow{x^k_{\text{ser}\_1}} + B^k_{\text{ser}\_1} \left[\Delta v^k_{1d}, \Delta v^k_{1q} \right]^T$$
$$\left[\Delta i^k_{1rd}, \Delta i^k_{1rq} \right]^T = C^k_{\text{ser}\_1} \Delta \overrightarrow{x^k_{\text{ser}\_1}} + D^k_{\text{ser}\_1} \left[\Delta v^k_{1d}, \Delta v^k_{1q} \right]^T$$
(11)

respectively. Then, $\mathbf{S}^l_{\text{ser}\_1}$ and $\mathbf{S}^k_{\text{ser}\_1}$ can be related by

$$\mathbf{Y}^k_{\text{ser}\_1} = -(C^k_{\text{ser}\_1}(sI - A^k_{\text{ser}\_1})^{-1}B^k_{\text{ser}\_1} + D^k_{\text{ser}\_1})$$
$$= \mathbf{R}(\theta)\mathbf{Y}^l_{\text{ser}\_1}\mathbf{R}^{-1}(\theta)$$
$$= -\mathbf{R}(\theta)(C^l_{\text{ser}\_1}(sI - A^l_{\text{ser}\_1})^{-1}B^l_{\text{ser}\_1} + D^l_{\text{ser}\_1})...$$
$$\mathbf{R}^{-1}(\theta). \quad (12)$$

The relationship between $\mathbf{S}^l_{\text{ser}\_1}$ and $\mathbf{S}^k_{\text{ser}\_1}$ can be derived from (12), shown as

$$A^k_{\text{ser}\_1} = \mathbf{R}(\theta)A^l_{\text{ser}\_1}\mathbf{R}^{-1}(\theta), \quad B^k_{\text{ser}\_1} = \mathbf{R}(\theta)B^l_{\text{ser}\_1}\mathbf{R}^{-1}(\theta)$$
$$C^k_{\text{ser}\_1} = \mathbf{R}(\theta)C^l_{\text{ser}\_1}\mathbf{R}^{-1}(\theta), \quad D^k_{\text{ser}\_1} = \mathbf{R}(\theta)D^l_{\text{ser}\_1}\mathbf{R}^{-1}(\theta)$$
(13)

which indicates that the SSM representations in different reference frames obey the same rotation operation as that of the impedance matrix reformulation.

The SSM of component #2 in the k-node reference frame, i.e., $\mathbf{S}^k_{\text{ser}\_2}$, is assumed as

$$\Delta \overset{\bullet}{\overrightarrow{x^k_{\text{ser}\_2}}} = A^k_{\text{ser}\_2} \Delta \overrightarrow{x^k_{\text{ser}\_2}} + B^k_{\text{ser}\_2} \begin{bmatrix} \Delta i^k_{2ld} \\ \Delta i^k_{2rd} \\ \Delta i^k_{2lq} \\ \Delta i^k_{2rq} \end{bmatrix}$$
$$\begin{bmatrix} \Delta v^k_{1d} \\ \Delta v^k_{2d} \\ \Delta v^k_{1q} \\ \Delta v^k_{2q} \end{bmatrix} = C^k_{\text{ser}\_2} \Delta \overrightarrow{x^k_{\text{ser}\_2}} + D^k_{\text{ser}\_2} \begin{bmatrix} \Delta i^k_{2ld} \\ \Delta i^k_{2rd} \\ \Delta i^k_{2lq} \\ \Delta i^k_{2rq} \end{bmatrix}. \quad (14)$$

Based on the time-domain CCM in Section II-B, $\mathbf{S}^k_{\text{ser}\_1}$ and $\mathbf{S}^k_{\text{ser}\_2}$ can be assembled as $\mathbf{S}^k_{\text{ser}}$ by (3), where $\overrightarrow{\Delta u_{\text{sys}}} = [\Delta i^k_{2rd}, \Delta i^k_{2rq}]^T$ and $\overrightarrow{\Delta y_{\text{sys}}} = [\Delta v^k_{2d}, \Delta v^k_{2q}]^T$. The composite SSM of Fig. 3(a) can then be represented as (4). Similar with the IMSO $\oplus'$, the SSMSO $\oplus$ is defined for the aforementioned

series assembling of the components' SSMs, shown as

$$\mathbf{S}_{\mathbf{ser}}^{k} = \mathbf{S}_{\mathbf{ser\_1}}^{k} \oplus \mathbf{S}_{\mathbf{ser\_2}}^{k} = \left(\mathbf{R}(\theta) \mathbf{S}_{\mathbf{ser\_1}}^{l} \mathbf{R}^{-1}(\theta) \right) \oplus \mathbf{S}_{\mathbf{ser\_2}}^{k}. \tag{15}$$

Commutative law is not satisfied for $\oplus$, since different reference node selections make the transition matrix inconsistent, whereas associative law is met, shown as

$$\mathbf{S}_{\mathbf{ser\_1}}^{l} \oplus \mathbf{S}_{\mathbf{ser\_2}}^{k} \oplus \mathbf{S}_{\mathbf{ser\_3}}^{m} = \mathbf{S}_{\mathbf{ser\_1}}^{l} \oplus \left(\mathbf{S}_{\mathbf{ser\_2}}^{k} \oplus \mathbf{S}_{\mathbf{ser\_3}}^{m} \right). \tag{16}$$

2) PROPOSED STATE–SPACE MODEL PARALLEL OPERATOR (SSMPO) ⊙

The SSMs of components/subsystems #1 and #2 in Fig. 3(b) are assumed to be $\mathbf{S}_{\mathbf{par\_1}}^{m}$ and $\mathbf{S}_{\mathbf{par\_2}}^{m}$, respectively, shown as

$$\Delta \overrightarrow{\dot{x}_{\mathrm{par\_1}}^{m}} = A_{\mathrm{par\_1}}^{m} \Delta \overrightarrow{x_{\mathrm{par\_1}}^{m}} + B_{\mathrm{par\_1}}^{m} \begin{bmatrix} \Delta i_{1\mathrm{rd}}^{m} \\ \Delta i_{1\mathrm{rq}}^{m} \end{bmatrix}$$

$$\begin{bmatrix} \Delta v_{1,2\mathrm{d}}^{3m'} \\ \Delta v_{1,2\mathrm{q}}^{3m'} \end{bmatrix} = C_{\mathrm{par\_1}}^{m} \Delta \overrightarrow{x_{\mathrm{par\_1}}^{m}} + D_{\mathrm{par\_1}}^{m} \begin{bmatrix} \Delta i_{1\mathrm{rd}}^{m} \\ \Delta i_{1\mathrm{rq}}^{m} \end{bmatrix} \tag{17}$$

and

$$\Delta \overrightarrow{\dot{x}_{\mathrm{par\_2}}^{m}} = A_{\mathrm{par\_2}}^{m} \Delta \overrightarrow{x_{\mathrm{par\_2}}^{m}} + B_{\mathrm{par\_2}}^{m} \begin{bmatrix} \Delta i_{2\mathrm{rd}}^{m} \\ \Delta i_{2\mathrm{rq}}^{m} \end{bmatrix}$$

$$\begin{bmatrix} \Delta v_{1,2\mathrm{d}}^{3m''} \\ \Delta v_{1,2\mathrm{q}}^{3m''} \end{bmatrix} = C_{\mathrm{par\_2}}^{m} \Delta \overrightarrow{x_{\mathrm{par\_2}}^{m}} + D_{\mathrm{par\_2}}^{m} \begin{bmatrix} \Delta i_{2\mathrm{rd}}^{m} \\ \Delta i_{2\mathrm{rq}}^{m} \end{bmatrix} \tag{18}$$

respectively. In order to assemble the two SSMs, one SSM should be inverted, e.g., the input and output variables of $\mathbf{S}_{\mathbf{par\_2}}^{m}$ are exchanged. To this end, a zero-valued virtual inductor L_{vir} is inserted at the right of subsystem #2. Its SSM is

$$\Delta \overrightarrow{\dot{x}_{\mathrm{vir}}^{m}} = A_{\mathrm{vir}}^{m} \Delta \overrightarrow{x_{\mathrm{vir}}^{m}} + B_{\mathrm{vir}}^{m} \begin{bmatrix} \Delta v_{1,2\mathrm{d}}^{3m''} \\ \Delta v_{1,2\mathrm{d}}^{3m} \\ \Delta v_{1,2\mathrm{q}}^{3m''} \\ \Delta v_{1,2\mathrm{q}}^{3m} \end{bmatrix}$$

$$\begin{bmatrix} -\Delta i_{2\mathrm{rd}}^{m} \\ \Delta i_{2\mathrm{rd}}^{m} \\ -\Delta i_{2\mathrm{rq}}^{m} \\ \Delta i_{2\mathrm{rq}}^{m} \end{bmatrix} = C_{\mathrm{vir}}^{m} \Delta \overrightarrow{x_{\mathrm{vir}}^{m}} + D_{\mathrm{vir}}^{m} \begin{bmatrix} \Delta v_{1,2\mathrm{d}}^{3m''} \\ \Delta v_{1,2\mathrm{d}}^{3m} \\ \Delta v_{1,2\mathrm{q}}^{3m''} \\ \Delta v_{1,2\mathrm{q}}^{3m} \end{bmatrix} \tag{19}$$

based on which $\mathbf{S}_{\mathbf{par\_2}}^{m}$ and $\mathbf{S}_{\mathbf{vir}}^{m}$ can be assembled as $\mathbf{S}_{\mathbf{par\_2}}^{m'}$ by (3), where $\Delta \overrightarrow{u_{\mathrm{sys}}} = [\Delta v_{1,2\mathrm{d}}^{3m}, \Delta v_{1,2\mathrm{q}}^{3m}]^{T}$, and $\Delta \overrightarrow{y_{\mathrm{sys}}} = [\Delta i_{2\mathrm{rd}}^{m}, \Delta i_{2\mathrm{rq}}^{m}]^{T}$. Then, the two parallel branches, i.e., $\mathbf{S}_{\mathbf{par\_1}}^{m}$ and $\mathbf{S}_{\mathbf{par\_2}}^{m'}$, can be further assembled as $\mathbf{S}_{\mathbf{par}}^{m}$ by (3), where $\Delta \overrightarrow{u_{\mathrm{stac}}} = [\Delta i_{1\mathrm{rd}}^{m}, \Delta i_{1\mathrm{rq}}^{m}, \Delta v_{1,2\mathrm{d}}^{3m}, \Delta v_{1,2\mathrm{q}}^{3m}]^{T}$, $\Delta \overrightarrow{y_{\mathrm{stac}}} = [\Delta v_{1,2\mathrm{d}}^{3m}, \Delta v_{1,2\mathrm{q}}^{3m}, \Delta i_{2\mathrm{rd}}^{m}, \Delta i_{2\mathrm{rq}}^{m}]^{T}$, $\Delta \overrightarrow{u_{\mathrm{sys}}} = [\Delta i_{3\mathrm{d}}^{m}, \Delta i_{3\mathrm{q}}^{m}]^{T}$, and $\Delta \overrightarrow{y_{\mathrm{sys}}} = [\Delta v_{1,2\mathrm{d}}^{3m}, \Delta v_{1,2\mathrm{q}}^{3m}]^{T}$.

Similar to the IMPO $\odot'$, the SSMPO $\odot$ is defined for the aforementioned parallel assembling of the components'
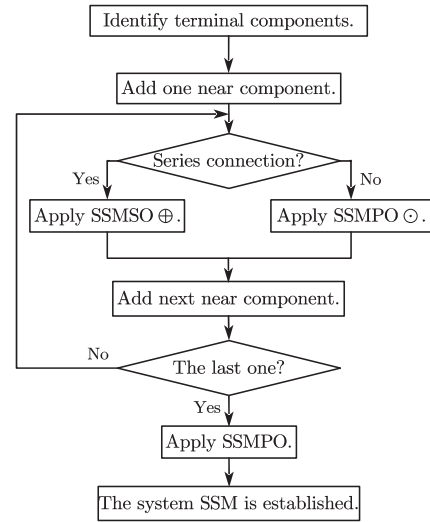

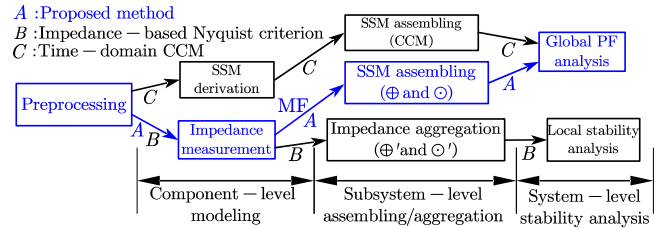**FIGURE 4.** Procedure of the proposed incremental state–space modeling method.

FIGURE 5. Roadmap of the proposed state–space modeling framework.

SSMs, shown as

$$\mathbf{S}_{\mathbf{par}}^{m} = \mathbf{S}_{\mathbf{par\_1}}^{m} \odot \mathbf{S}_{\mathbf{par\_2}}^{m}. \tag{20}$$

Both associative law and commutative law are satisfied for the SSMPO ⊙, shown as

$$\mathbf{S}_{\mathbf{par\_1}}^{m} \odot \mathbf{S}_{\mathbf{par\_2}}^{m} \odot \mathbf{S}_{\mathbf{par\_3}}^{m} = \mathbf{S}_{\mathbf{par\_1}}^{m} \odot \left(\mathbf{S}_{\mathbf{par\_3}}^{m} \odot \mathbf{S}_{\mathbf{par\_2}}^{m} \right). \tag{21}$$

3) PROPOSED INCREMENTAL STATE–SPACE MODELING METHOD

Fig. 4 shows the implementation procedure of the proposed incremental state–space modeling method. The terminal components are first identified. Then, the components are assembled together one by one. Specifically, if the interconnection relationship is series connection, the SSMSO $\oplus$ is applied. Otherwise, the SSMPO $\odot$ is applied. The last component is regarded as parallel with the assembled subsystem, i.e., the SSMPO $\odot$ is employed in the last step.

C. PROPOSED STATE–SPACE MODELING FRAMEWORK

Based on Sections III-A and III-B, the roadmap of the proposed state–space modeling framework is drawn as the blue line A in Fig. 5, where the roadmaps of the other two mature modeling methods, i.e., the impedance-based Nyquist

criterion and the time-domain CCM, are drawn as lines B and C, respectively. At the preprocessing stage, power flow calculation is performed in all the three roadmaps to obtain the operation points of the VSCs, which provides the basis for the further SSM derivation or admittance measurement of the VSCs. Then, the overall system is divided into individual components for further implementations of the three modeling methods.

Roadmap A illustrates that the proposed method requires only the measured AFRs/IFRs for component-level reduced-order state–space modeling. At the subsystem level, it can combine these SSMs similarly to impedance aggregation. Thanks to the proposed SSMOs, the combination of two components/subsystems can ignore the global picture of the studied system, which is advantageous especially when system topology changes or new/existing VSCs are installed/removed. Furthermore, it enables global PF analysis at the system level. The proposed modeling framework integrates the strengths of the impedance-based Nyquist criterion and the time-domain CCM across the three hierarchical levels. This approach aims to align the needs of both device manufacturers and system planners. Notably, it allows eigenvalue and PF analyses using just the IFRs of individual components.

IV. IMPLEMENTATION OF PROPOSED MODELING FRAMEWORK

In this section, the proposed modeling framework is implemented. The ROMs of the VSCs and cables are first established, followed by the incremental system state–space modeling.

A. BLACK BOX-BASED REDUCED-ORDER MODELING OF VSCS AND CABLES

1) REDUCED-ORDER MODELING OF VSCS

The four VSCs in Fig. 1(a) are assumed as the same. Their control scheme is shown in Fig. 17 in Appendix A. In addition, their circuit and controller parameters can be found in Table 2 in Appendix A. Bode diagrams of the frequency scanning-based dq-domain low-frequency and high-frequency AFRs, i.e., $\mathbf{Y}_{mea}^{low}$ and $\mathbf{Y}_{mea}^{high}$, are plotted in Figs. 6(a) and 7(a), respectively. It can be seen that $\mathbf{Y}_{mea}^{low}$ and $\mathbf{Y}_{mea}^{high}$ highly agree with the analytical ones, i.e., $\mathbf{Y}_{ana}^{low}$ and $\mathbf{Y}_{ana}^{high}$, respectively. In [28], the 6th-order and 14th-order models are generated by applying the MF algorithm on the AFRs in the whole frequency range from 1 Hz to 2.5 kHz. The fitting results in [28] indicate that the fitted low-order model tends to preferentially reproduce the current control loop-dominated high-frequency modes, which is satisfying if the high-frequency modes are only of concern. However, if the PLL-dominated low-frequency modes are only of concern, a higher order has to be selected, which may be cumbersome and not computationally efficient. To this end, a frequency range-oriented reduced-order modeling method of VSCs is conceived in this article. In detail, $\mathbf{Y}_{mea}^{low}$ and $\mathbf{Y}_{mea}^{high}$ are individually fitted by the MF algorithm,
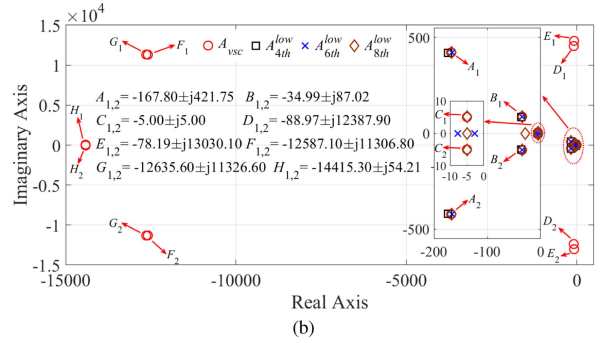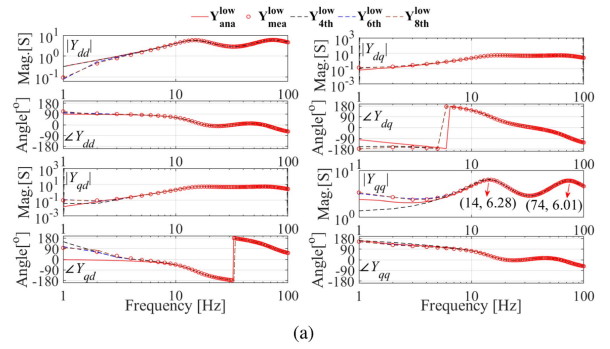

FIGURE 6. Fitting results of the measured dq-domain AFRs of the VSCs in low-frequency range from 1 to 100 Hz. (a) Bode plots. (b) Eigenvalue distributions.
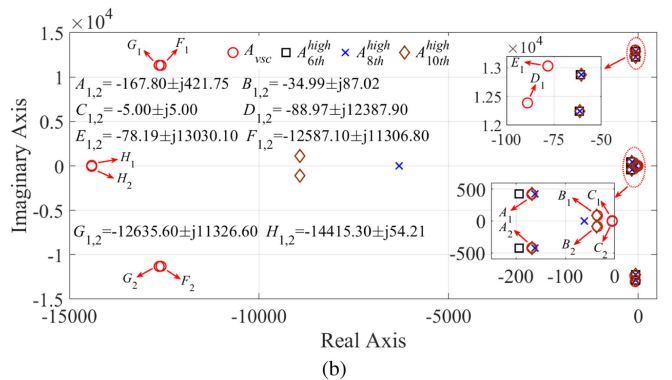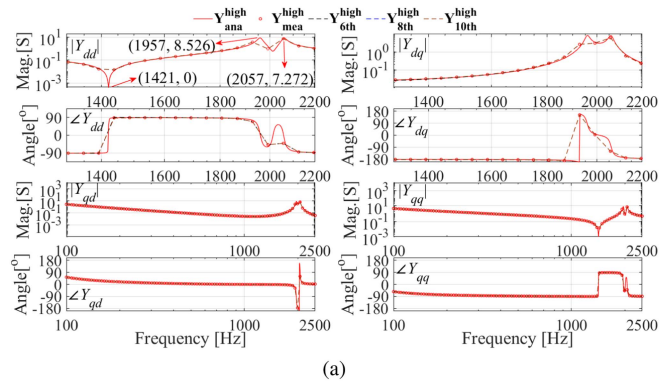

FIGURE 7. Fitting results of the measured dq-domain AFRs of the VSCs in high-frequency range from 100 Hz to 2.5 kHz. (a) Bode plots. (b) Eigenvalue distributions.

where the fitting order gradually increases until the fitting error defined by (9) is smooth.

Fig. 6(a) plots the Bode diagrams of the fitted 4th-, 6th-, and 8th-order transfer function matrices (i.e., $\mathbf{Y}_{4th}^{low}$, $\mathbf{Y}_{6th}^{low}$, and $\mathbf{Y}_{8th}^{low}$) for the low-frequency AFRs. Their fitting errors are 0.1812 S, 0.0308 S, and 0.0210 S, respectively, which gradually decrease as the fitting order increases. Furthermore, Fig. 6(b) draws the eigenvalue distributions of these ROMs (i.e., A_{4th}^{low}, A_{6th}^{low}, and A_{8th}^{low}) and the full 16th-order SSM (i.e., A_{vsc}). It can be observed that the three ROMs can reproduce the low-frequency eigenvalue pairs $A_{1,2}$ and $B_{1,2}$. In addition, another low-frequency eigenvalue pair $C_{1,2}$ is misidentified by the 6th-order model as a pair of real eigenvalues, which is instead accurately identified by the 8th-order model. Since the 8th-order model can reproduce all the eigenvalues below 100 Hz, it will be used in the following subsystem-level assembling and system-level stability analysis.

Fig. 7(a) plots the Bode diagrams of the fitted 6th-, 8th-, and 10th-order transfer function matrices (i.e., $\mathbf{Y}_{6th}^{high}$, $\mathbf{Y}_{8th}^{high}$, and $\mathbf{Y}_{10th}^{high}$) for the high-frequency AFRs. Their fitting errors defined by (9) are 0.0162 S, 0.0010 S, and 2.3604×10^{-5} S, respectively, which gradually decrease as the fitting order increases. Since the current control loop-dominated high-frequency AFRs are symmetric, i.e., the diagonal and off-diagonal elements of the admittance matrix are the same and opposite, respectively, full views of Y_{qd} and Y_{qq} are given to illustrate the global fitting capability, whereas zoomed views of Y_{dd} and Y_{dq} are given to illustrate the local fitting capability of LCL-filter resonance frequencies. In general, the fitting accuracy is satisfying for the whole high-frequency range except two narrow frequency ranges around the magnitude valley 1421 Hz and the magnitude peaks (i.e., 1957 Hz and 2057 Hz), respectively, which is due to the limited measurement resolution. Furthermore, Fig. 7(b) draws the eigenvalue distributions of these ROMs (i.e., A_{6th}^{high}, A_{8th}^{high}, and A_{10th}^{high}) and the full 16th-order SSM (i.e., A_{vsc}). The three ROMs can reproduce the high-frequency eigenvalue pairs $D_{1,2}$ and $E_{1,2}$, and their reproduction capabilities are almost the same, although slight discrepancies between the real parts exist. However, the reproduction capabilities of the 8th- and 10th-order models for the low-frequency eigenvalue pair $A_{1,2}$ are better than that of the 6th-order model. The unique merit of the 10th-order model is that another low-frequency eigenvalue pair $B_{1,2}$ can be captured. It can be seen that the two pairs of low-frequency eigenvalues (i.e., $A_{1,2}$ and $B_{1,2}$) can be identified from the measured high-frequency AFRs with the help of the MF algorithm. By comparing Fig. 7(a) and (b), it can be seen that $D_{1,2}$ and $E_{1,2}$ are related with the LCL-filter resonance frequencies. Similar with Fig. 7(a), the discrepancies between $D_{1,2}$, $E_{1,2}$ and their fitting values result from the limited measurement resolution around the LCL-filter resonance frequencies. Since the 6th-order model can reproduce the dominant eigenvalues above 100 Hz, it can be used in the subsystem-level assembling and system-level stability analysis.
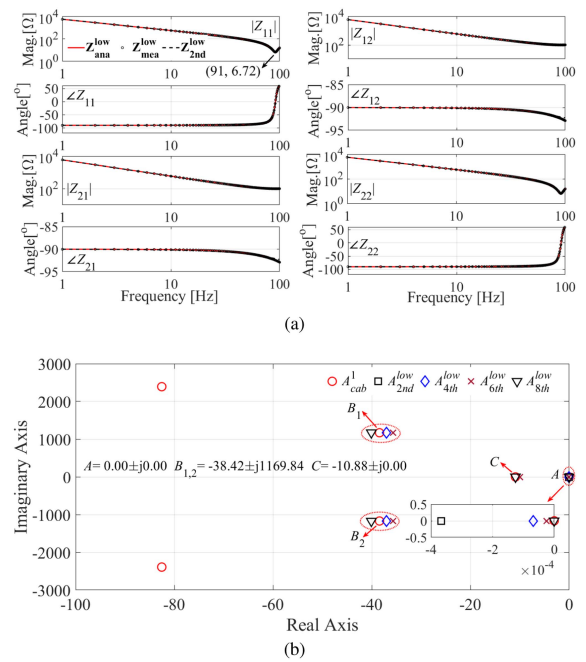

FIGURE 8. Fitting results of the measured *abc*-domain IFRs of the cables in low-frequency range from 1 to 100 Hz. (a) Bode plots. (b) Eigenvalue distributions.

2) REDUCED-ORDER MODELING OF CABLES

The single-Π distributed-parameter circuit model of the cables shown in Fig. 1(a) can be represented as the equivalent multiple-Π lumped-parameter RLC circuit model, where more parallel branches and more cascaded Π sections can achieve better reproduction results of the frequency-dependent characteristics and high-frequency impedance characteristics, respectively [21], [23]. This enhanced accuracy is crucial for studying the small-signal interactions between devices or the system's transient behaviors. The cable parameters can be found in [29]. Fig. 8(a) shows that the measured low-frequency IFRs $\mathbf{Z}_{mea}^{low}$ highly agree with the analytical ones $\mathbf{Z}_{ana}^{low}$ (i.e., the low-frequency responses of Z_{11}, Z_{12}, Z_{21}, and Z_{22}). The fitting errors of the fitted 2nd-, 4th-, 6th-, and 8th-order transfer function matrices (i.e., $\mathbf{Z}_{2nd}^{low}$, $\mathbf{Z}_{4th}^{low}$, $\mathbf{Z}_{6th}^{low}$, and $\mathbf{Z}_{8th}^{low}$) are 4.7362, 0.0225, 0.0071, and 5.7039×10^{-4} Ω, respectively, which gradually decrease as the fitting order increases. Only the Bode diagram of $\mathbf{Z}_{2nd}^{low}$ is plotted for simplicity. Furthermore, Fig. 8(b) draws the eigenvalue distributions of these ROMs (i.e., A_{2nd}^{low}, A_{4th}^{low}, A_{6th}^{low}, and A_{8th}^{low}) and the 721th-order full-order model (FOM) ($80 \times (8 + 1) + 1 = 721$), i.e., A_{cab}^{1}. All of the four ROMs can reproduce the real eigenvalue located at the origin $A = 0.00 + j0.00$. In addition, A_{4th}^{low}, A_{6th}^{low}, and A_{8th}^{low} can reproduce a pair of complex eigenvalues located at $B_{1,2} = -38.42 \pm j1169.84$, of which the imaginary parts correspond to $\frac{1169.84}{2\pi} = 186.19$ Hz. It means that, with the help of the MF algorithm, the magnitude peak located at 186 Hz can be captured based on only the IFRs below 100 Hz. Furthermore, A_{6th}^{low} and A_{8th}^{low} can reproduce the real eigenvalue located at $C = -10.88 + j0.00$. The
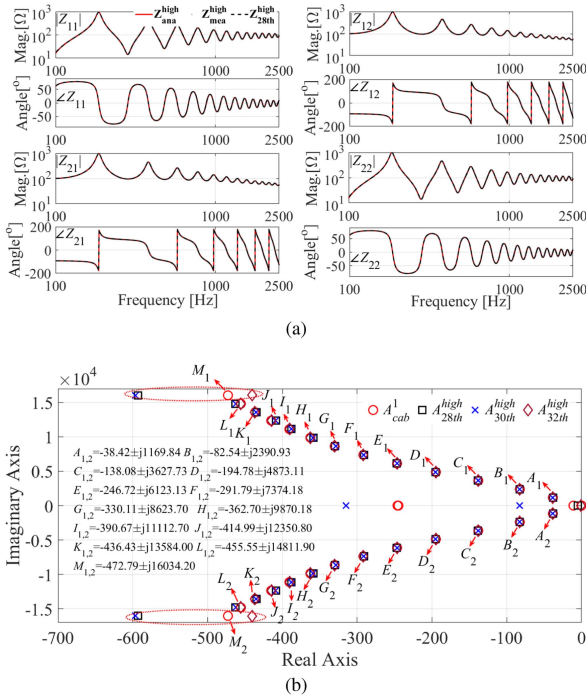
(a)

(b)

FIGURE 9. Fitting results of the measured abc-domain IFRs of the cables in high-frequency range from 100 Hz to 2.5 kHz. (a) Bode plots. (b) Eigenvalue distributions.

8th-order model will be used in the following subsystem-level assembling and system-level stability analysis.

Fig. 9(a) shows that the measured high-frequency IFRs $\mathbf{Z}_{mea}^{high}$ highly agree with the analytical ones $\mathbf{Z}_{ana}^{high}$ (i.e., the high-frequency responses of Z_{11}, Z_{12}, Z_{21}, and Z_{22}). The fitting error when the order is not lower than 28th is small enough and acceptable. Since there are 12 magnitude peaks from 100 Hz to 2.5 kHz, the minimum order can be intuitively deduced to be not lower than 24th in order to capture all of the 12 peaks. Only the Bode diagram of $\mathbf{Z}_{28th}^{high}$ is plotted in Fig. 9(a) for simplicity. Furthermore, Fig. 9(b) draws the eigenvalue distributions of three ROMs (i.e., A_{28th}^{high}, A_{30th}^{high}, and A_{32th}^{high}) and the 721th-order FOM (i.e., A_{cab}^{1}). It can be observed that the three ROMs reproduce almost the same 12 pairs of complex eigenvalues $A_{1,2}$-$L_{1,2}$. Note that the 13th pair of complex eigenvalues $M_{1,2}$ above 2.5 kHz are also captured, although the damping ratios are slightly overestimated. The 28th-order model can be used in the subsystem-level assembling and system-level stability analysis.

Based on the abovementioned fitted abc-domain SSM for the single-phase ac cable, the dq-domain SSM for the corresponding three-phase ac cable can be further derived, of which the eigenvalues can be further calculated.

Since the employed order reduction method captures both the dominant and nondominant poles in the frequency range of interest, the effects of the in-band nondominant poles of the VSCs and cables on the in-band dominant poles of the closed-loop system composed by the VSCs and cables can be preserved.
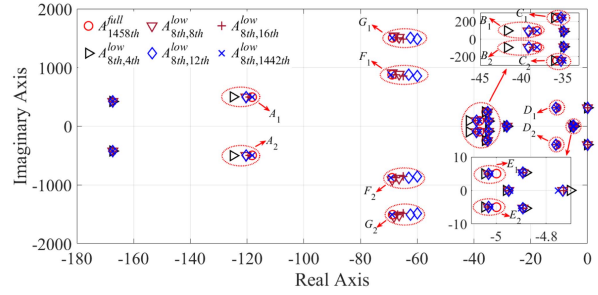

FIGURE 10. Eigenvalues of the assembled SSMs obtained by applying the proposed SSMSO at node N_1 on VSC #1 and cable #5.

B. INCREMENTAL SYSTEM STATE–SPACE MODELING USING SSMOS

The transformers T_1-T_4 in Fig. 1 boost the voltage from 575 V to 33 kV, and the transformer T_5 boosts the voltage from 33 to 330 kV. The power flow obtained in MATLAB/Simulink environment shows that, if point of common coupling (PCC) is regarded as the reference node, the voltage phasors at nodes N_1-N_4 and PCC are $1203.8 / -2.5272°$, $1203.8 / -2.5272°$, $1203.8 / -2.5272°$, $1203.8 / -2.5272°$, and $44377.0 / 0°$, respectively. Based on the power flow results together with the fitted reduced-order SSMs of the VSCs and cables in Section IV-A, the SSM of the inverter-based power system can be incrementally established by recursively applying the proposed SSMSO four times at nodes N_1-N_4 and SSMPO four times at PCC. For the sake of simplicity, only the low-frequency ROMs of the VSCs and cables will be assembled, while their high-frequency ROMs can also be assembled in a similar manner.

1) SSMSO APPLIED AT NODES N_1-N_4

The eigenvalues of the composite SSM of VSC #1 and cable #5 obtained by assembling the 8th-order SSM of the VSC in Fig. 6(b) and the various ROMs of the cable in Fig. 8(b) based on (15) are plotted in Fig. 10, where the eigenvalues of the corresponding full 1458th-order SSM A_{1458th}^{full} are also drawn ($16 + 2 \times 721 = 1458$). It should be noted that the effect of the transformer T_1 on the SSM assembling and impedance aggregation should be taken into consideration, i.e., $\overrightarrow{i_{5l}} = \frac{1}{K_T}\overrightarrow{i_{1r}}$ and $\overrightarrow{v_1^{5\prime}} = K_T \overrightarrow{v_1^5}$ in Fig. 1(b), where $K_T = 57.3913$ is the transformer ratio. It can be observed that all of the established ROMs can preserve the dominant low-frequency modes $A_{1,2}$, $B_{1,2}$, $C_{1,2}$, and $E_{1,2}$. In addition, the established ROMs using the 12th- and 16th-order cable's models can further capture other low-frequency modes $D_{1,2}$, $F_{1,2}$, and $G_{1,2}$. The effectiveness of the proposed SSMSO is thus validated.

2) SSMPO APPLIED AT PCC

Since cable #9 is connected with the utility grid, its SSM should be extracted from one-end short-circuit abc-domain AFRs, which can be calculated as $Z_{11}/(Z_{11}^2 - Z_{12}^2)$. 6th and 8th orders are used for the curve fitting. On its basis, the
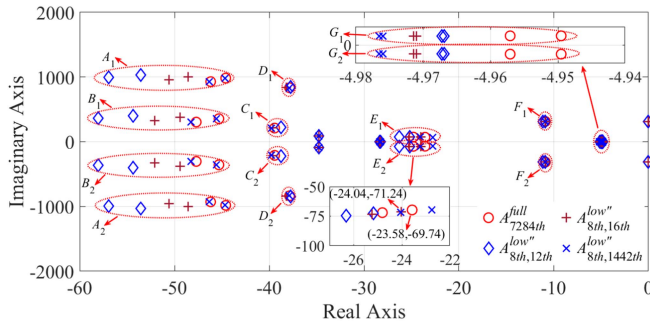
FIGURE 11. Eigenvalues of the assembled system SSM obtained by applying the proposed SSMPO at PCC on the assembled four parallel VSC branches and cable #9.

eigenvalues of the composite SSM of the four VSC branches and cable #9 obtained by (20) are plotted in Fig. 11, where the eigenvalues of the corresponding full 7284th-order SSM A_{7284th}^{full} are also drawn ($5838 + 2 + 1442 + 2 = 7284$). It can be observed that all of the eigenvalues of A_{7284th}^{full} in the low-frequency range can be captured by the ROMs, and the reproduction capability increases when the fitting order increases.

V. BLACK BOX-BASED PF ANALYSIS AND VERIFICATION

In this section, the sizes, eigenvalues, and PF results of the derived system's ROMs in Section IV-B are compared to those of the FOMs, followed by the time-domain simulation verification in MATLAB/Simulink environment.

A. COMPARISONS BETWEEN THE PROPOSED AND STATE–SPACE-BASED MODELING METHOD

Based on the derived ROM $A_{8th,16th}^{low''}$ and the FOM A_{7284th}^{full} in Fig. 11 for the four-branch-based power system in Fig. 1, when new branches are integrated, the system's ROM and FOM can be incrementally derived with the help of the proposed SSMPO. Fig. 12 shows the distributions of the non-zero values of the system SSMs when the number of the total parallel branches N_{branch} is 4 and 32. Both the FOMs and ROMs are sparse and diagonally dominant. The ratios of the element numbers of the derived ROMs and the FOMs are 0.0863% and 0.1123% under the two configurations. Furthermore, the ratios of the nonzero-element numbers of the derived ROMs and the FOMs are 3.36% and 26.25% under the two configurations. The computational burdens of the subsequent eigenvalues calculation and PF analysis using the ROMs can thus be released. The proposed SSMOs can incrementally derive new system SSM based on the existing system SSM when new components are put into operation.

Fig. 13 shows the eigenvalues loci of the FOMs and ROMs when N_{branch} increases from 4 to 32 with step size 4. It can be observed that there are mainly eight pairs of low-frequency modes, i.e., $A_{1,2}$-$H_{1,2}$. The eigenvalues of the ROMs generally agree with those of the FOMs, although slight discrepancies exist in the real parts of $A_{1,2}$ and $B_{1,2}$. Furthermore, the modes
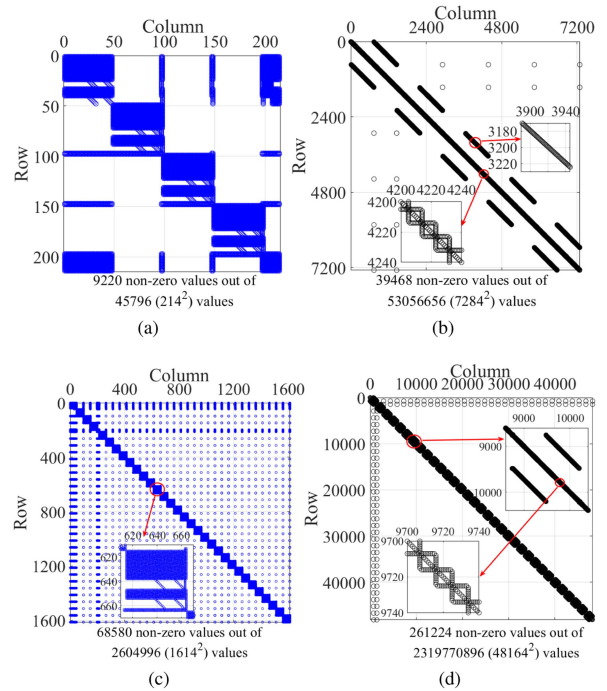

FIGURE 12. Distributions of the nonzero values of the system SSMs. (a) ROM and (b) FOM when $N_{branch} = 4$. (c) ROM and (d) FOM when $N_{branch} = 32$.
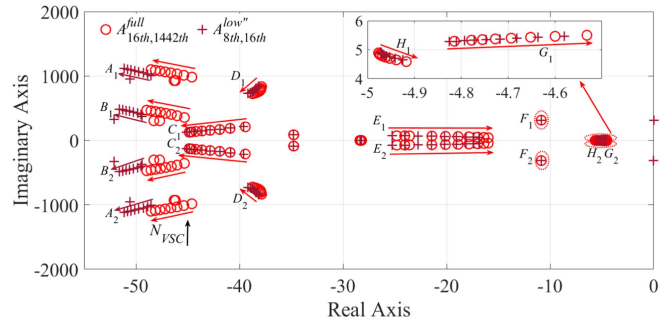

FIGURE 13. Eigenvalues loci of the full-order and reduced-order SSMs when N_{branch} increases from 4 to 32 with step size 4.

TABLE 1. Summary of the Dominant Modes in Fig. 13 and the Simulation Results in Fig. 15

Branches	Modes	ROMs	FOMs	EMT simulation (dq domain)
4	$B_{1,2}$	$-49.40 \pm j374.93\rightarrow$	$-45.32 \pm j356.05\rightarrow$	$(\frac{370.71}{2\pi}$ Hz$\rightarrow$, 8.35A)
	$C_{1,2}$	$-39.62 \pm j216.56\rightarrow$	$-39.44 \pm j210.66\rightarrow$	$(\frac{216.77}{2\pi}$ Hz$\rightarrow$, 16.67A)
	$E_{1,2}$	$-24.04 \pm j71.24\rightarrow$	$-23.58 \pm j69.74\rightarrow$	$(\frac{75.54}{2\pi}$ Hz$\rightarrow$, 118.16A)
	$G_{1,2}$	$-4.81 \pm j5.29\rightarrow$	$-4.81 \pm j5.29\rightarrow$	$(\frac{6.28}{2\pi}$ Hz$\rightarrow$, 63.20A)
32	$B_{1,2}$	$-51.58 \pm j486.25\uparrow$	$-48.97 \pm j470.35\uparrow$	$(\frac{474.38}{2\pi}$ Hz$\uparrow$, 6.79A)
	$C_{1,2}$	$-45.13 \pm j129.19\downarrow$	$-44.85 \pm j126.54\downarrow$	$(\frac{138.23}{2\pi}$ Hz$\downarrow$, 49.95A)
	$E_{1,2}$	$-16.87 \pm j45.20\downarrow$	$-15.98 \pm j41.87\downarrow$	$(\frac{47.12}{2\pi}$ Hz$\downarrow$, 86.94A)
	$G_{1,2}$	$-4.58 \pm j5.46\uparrow$	$-4.53 \pm j5.50\uparrow$	$(\frac{12.56}{2\pi}$ Hz$\uparrow$, 67.50A)

$B_{1,2}$, $C_{1,2}$, $E_{1,2}$, and $G_{1,2}$ are summarized in Table 1, which indicates that, for both the ROMs and FOMs, the imaginary parts of $B_{1,2}$ and $G_{1,2}$ increase, whereas the imaginary parts of $C_{1,2}$ and $E_{1,2}$ decrease. In addition, the most dominant eigenvalue pair $G_{1,2}$ moves rightward as N_{branch} increases, which indicates that the system becomes less stable. This
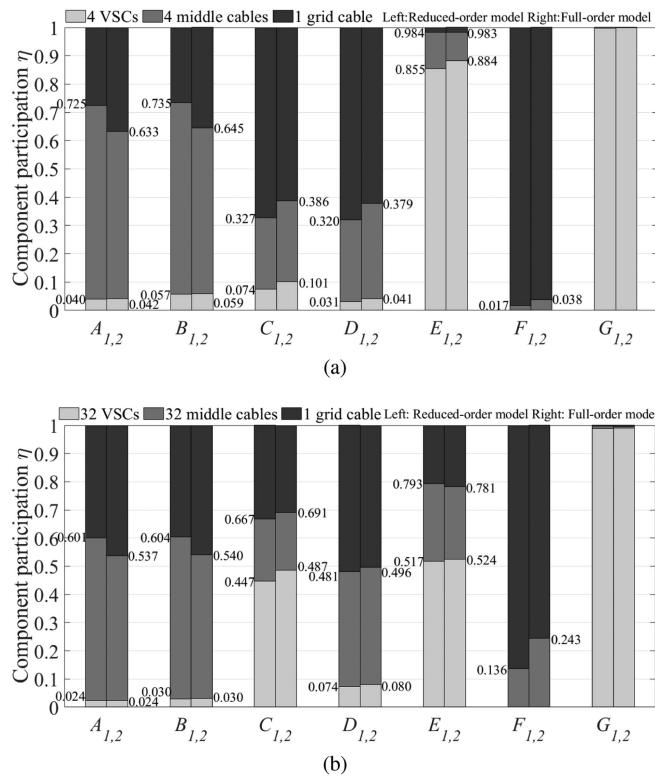
(a)

(b)

FIGURE 14. PF analysis results of the ROMs and FOMs in Fig. 13 for modes $A_{1,2}$-$G_{1,2}$ when (a) $N_{\text{branch}} = 4$ and (b) $N_{\text{branch}} = 32$.

FIGURE 15. Time-domain simulation results of three-phase output currents of VSC #1 in Fig. 1. (a) Waveform and (b) DFT when $N_{\text{branch}} = 4$. (c) Waveform and (d) DFT when $N_{\text{branch}} = 32$.

It should be noted that the proposed state–space modelling method cannot further identify the problematic controller parameters, since the VSCs are black boxes and the generated state variables have no physical meaning. If these VSCs are gray boxes, i.e., their interal control structures are known, control parameters can be identified from the measured dq-domain AFRs [30], and parameter-level PF analysis can be further performed.

eigenvalue behavior agrees with that weak grid tends to make the IBR-based power systems less stable.

B. PF ANALYSIS

The PF analysis results are shown in Fig. 14. It can be observed that, for both cases, the PF analysis results using the ROMs are similar as those using the FOMs. In detail, all of the three groups of components (e.g., VSCs, middle cables, and grid cable) contribute to modes $A_{1,2}$-$E_{1,2}$, whereas only the middle cables and grid cable contribute to the modes $F_{1,2}$. The participation of the VSCs in the modes $G_{1,2}$ is nearly 1. On the one hand, as N_{branch} increases from 4 to 32, both the ROMs and FOMs show that the contributions of VSCs to modes $A_{1,2}$, $B_{1,2}$, and $G_{1,2}$ slightly decrease, whereas their contribution to modes $E_{1,2}$ significantly decreases. On the other hand, their contributions to modes $C_{1,2}$ and $D_{1,2}$ significantly and slightly increase, respectively. As for the middle cables, their contributions to modes $A_{1,2}$-$C_{1,2}$ slight decrease, whereas their contributions to modes $D_{1,2}$-$F_{1,2}$ slight increase. Finally, as for the grid cable, its contribution to $A_{1,2}$, $B_{1,2}$, and $E_{1,2}$ slightly increases. In addition, its contribution to $C_{1,2}$ largely decreases and to $D_{1,2}$ and $F_{1,2}$ slightly decreases. Based on the abovementioned comparative analysis, it can be concluded that the black box-based ROMs suffice for the component-level PF calculation, i.e., the contributions of individual VSCs and cables to the each system mode can be obtained.
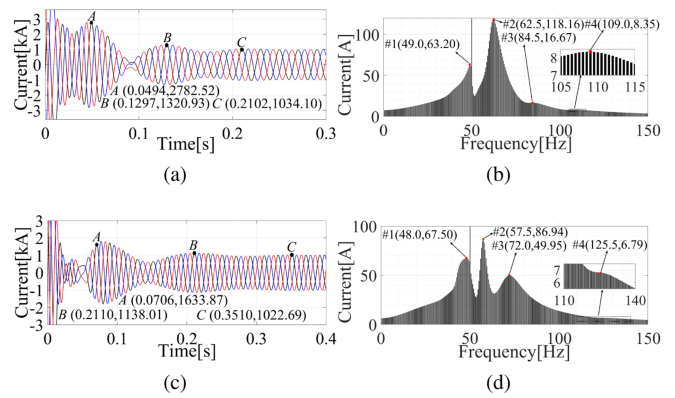
C. TIME-DOMAIN SIMULATION VERIFICATION

In order to verify the correctness of the eigenvalues identified by the ROMs in Section V-A, Fig. 15 shows the time-domain simulation results of three-phase output currents of VSC #1 for the two cases, i.e., the number of paralleled branches is 4 and 32, respectively. Since the simulation results for VSCs #2, #3, and #4 are the same as that for VSC #1 due to the uniform control strategy adopted for all VSCs, only the simulation results of VSC #1 are presented as a representative example to avoid redundancy and for brevity. The DFT is implemented on the time-domain waveform during the first 2 s, and corresponding DFTs are plotted. The resolution is thus 0.5 Hz. It can be observed that, besides the 50-Hz fundamental component, there are four resonance frequencies below 150 Hz. Their information is summarized in the last column in Table 1. It should be noted that the abc-domain frequency points in Fig. 15(b) and (d) are shifted by 50 Hz in order to be expressed in dq-domain in Table 1. It can be observed that, as N_{branch} increases from 4 to 32, the $B_{1,2}$ ($G_{1,2}$)-related resonance frequency #4 (#1) obtained by the time-domain simulation increases from 370.71 (6.28) to 474.38 (12.56) rad/s. On the other hand, the $C_{1,2}$ ($E_{1,2}$)-related resonance frequency #3 (#2) obtained by the time-domain simulation decreases from 216.77 (78.54) to 138.23 (47.12) rad/s. The trends agree with the imaginary parts of the eigenvalues of the ROMs and FOMs. The feasibility of the established black box-based ROMs for component-level stability analysis is thus verified.
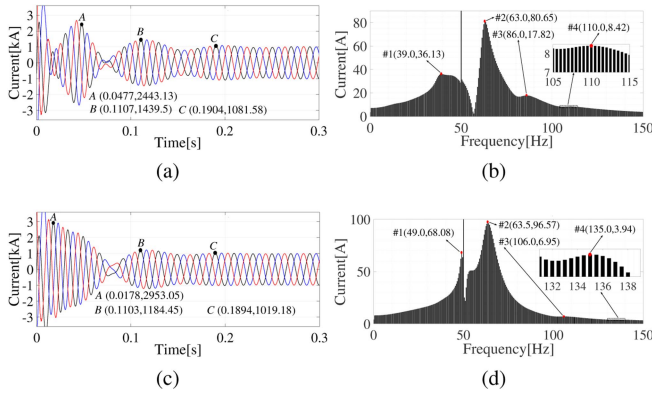
FIGURE 16. Time-domain simulation results of three-phase output currents of VSC #1 in Fig. 1 when $N_{branch} = 4$. (a) Waveform and (b) DFT as the PLL parameters of the four VSCs are increased to $K_{ppll} = 40$ rad/(Vs) and $K_{ipll} = 800$ rad/(Vs^2). (c) Waveform and (d) DFT as the length of the five cables is decreased to 80 km.

FIGURE 17. Control scheme of the LCL-filtered grid-connected VSC with current control loop and PLL.

TABLE 2. Circuit and Controller Parameters of the VSCs in Fig. 1(a)

Parameter	Value	Parameter	Value
V_{dc}	1150 V	L_{f2}	250 μH
V_g	330 kV	C_f	50 μF
ω_1	100π rad/s	K_{pi}	1.7391×10^{-4} Ω
f_s	5.0 kHz	K_{ii}	0.0348 Ω/s
f_{sw}	2.5 kHz	K_{ppll}	10 rad/(Vs)
R_{f1}	1 mΩ	K_{ipll}	50 rad/(Vs^2)
L_{f1}	250 μH	I_{2d}^{ref}	1.0 kA
R_{f2}	1 mΩ	I_{2q}^{ref}	0

Furthermore, in order to verify the correctness of the PF analysis results in Section V-B, Fig. 16(a) and (b) shows the time-domain simulation results of three-phase output currents of VSC #1 and its DFT, respectively, as the PLL parameters of the four VSCs are increased to $K_{ppll} = 40$ rad/(Vs) and $K_{ipll} = 800$ rad/(Vs^2). Compared to Fig. 15(b), it can be seen from Fig. 16(b) that the peak #1 [corresponding to the modes $G_{1,2}$ in Fig. 14(a)] experiences the largest variation from 49.0 to 39.0 Hz. This simulation result indicates that the four VSCs significantly contribute to the modes $G_{1,2}$, which agrees with the PF analysis result in Fig. 14(a). Similarly, Fig. 16(c) and (d) shows the time-domain simulation results of three-phase output currents of VSC #1 and its DFT, respectively, as the length of the five cables is decreased to 80 km. Compared to Fig. 15(b), it can be seen from Fig. 16(d) that the peaks #3 and #4 [corresponding to the modes $C_{1,2}$ and $B_{1,2}$ in Fig. 14(a)] experiences the largest variations from 84.5 to 106.0 Hz and from 109.0 to 135.0 Hz, respectively. Differently, the peaks #1 and #2 [corresponding to the modes $G_{1,2}$ and $E_{1,2}$ in Fig. 14(a)] are kept almost unchanged. These simulation results indicate that the five cables significantly contribute to the modes $C_{1,2}$ and $B_{1,2}$ and slightly contribute to the modes $G_{1,2}$ and $E_{1,2}$, which agrees with the PF analysis result in Fig. 14(a).

VI. CONCLUSION

This article presents a black box-based incremental reduced-order state–space modeling framework for inverter-based power systems. This framework aids in accurately identifying the state–space models at the component modeling phase. It also streamlines the assembly process during subsystem/component integration and reduces computational demands during the system PF analysis. The ROMs of individual components (e.g., VSCs and cables) are first identified from the components' measured AFRs/IFRs in the frequency rang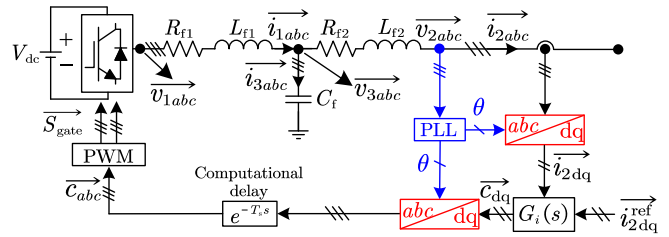e of interest with the help of the MF algorithm, which are then incrementally assembled based on the proposed SS-MOs (i.e., SSMSO and SSMPO). Time-domain simulation results obtained in the MATLAB/Simulink environment verify that the dominant system modes and PFs of individual components on these dominant modes can be captured by the proposed modeling framework. The merits of the proposed modeling framework can be summarized as follows. Compared to the state–space modeling method based on the conventional time-domain CCM, the proposed modeling framework does not require the internal structure and parameters of individual components. Compared to the conventional aggregation method for the components' impedance models, the proposed modeling framework can preserve components' dynamics with the help of the proposed SSMOs. Furthermore, the proposed SSMOs can incrementally derive the system SSM without considering the global picture of the studied system, which is advantageous especially when system topology changes or new/existing VSCs are installed/removed.

APPENDIX A
CONTROL SCHEME AND PARAMETERS OF THE VSCS

Fig. 17 shows the control scheme of the LCL-filtered grid-connected VSC under dq-domain current control mode with current control loop in black tracking current reference $\overrightarrow{i_{2dq}^{ref}}$ and PLL in blue tracking phase angle of terminal voltage $\overrightarrow{v_{2abc}}$. T_s denotes the sampling period. $\overrightarrow{C_{dq}}$ and $\overrightarrow{C_{abc}}$ denote the current PI controller's output represented within the dq and abc reference frames, respectively. The four VSCs in Fig. 1(a) are assumed as the same, and their circuit and controller parameters are listed in Table 2.

REFERENCES

[1] B. Kroposki et al., "Achieving a 100% renewable grid: Operating electric power systems with extremely high levels of variable renewable energy," *IEEE Power Energy Mag.*, vol. 15, no. 2, pp. 61–73, Mar./Apr. 2017.

[2] F. Blaabjerg, Z. Chen, and S. B. Kjaer, "Power electronics as efficient interface in dispersed power generation systems," *IEEE Trans. Power Electron.*, vol. 19, no. 5, pp. 1184–1194, Sep. 2004.

[3] N. Hatziargyriou et al., "Definition and classification of power system stability revisited & extended," *IEEE Trans. Power Syst.*, vol. 36, no. 4, pp. 3271–3281, Jul. 2021.

[4] N. Pogaku, M. Prodanovic, and T. C. Green, "Modeling, analysis and testing of autonomous operation of an inverter-based microgrid," *IEEE Trans. Power Electron.*, vol. 22, no. 2, pp. 613–625, Mar. 2007.

[5] M. Rasheduzzaman, J. A. Mueller, and J. W. Kimball, "An accurate small-signal model of inverter-dominated islanded microgrids using dq reference frame," *IEEE Trans. Emerg. Sel. Topics Power Electron.*, vol. 2, no. 4, pp. 1070–1080, Dec. 2014.

[6] G. Gaba, S. Lefebvre, and D. Mukhedkar, "Comparative analysis and study of the dynamic stability of AC/DC systems," *IEEE Trans. Power Syst.*, vol. 3, no. 3, pp. 978–985, Aug. 1988.

[7] N. Kroutikova, C. A. Hernandez-Aramburo, and T. C. Green, "State-space model of grid-connected inverters under current control mode," *IET Electric Power Appl.*, vol. 1, no. 3, pp. 329–338, May 2007.

[8] Ö. C. Sakinci and J. Beerten, "Impact of PLL dynamics on the small-signal stability of the MMC using dynamic phasor modeling in the ABC frame," *Electric Power Syst. Res.*, vol. 189, 2020, Art. no. 106729.

[9] D. Yang and X. Wang, "Unified modular state-space modeling of grid-connected voltage-source converters," *IEEE Trans. Power Electron.*, vol. 35, no. 9, pp. 9700–9715, Sep. 2020.

[10] Y. Wang, X. Wang, Z. Chen, and F. Blaabjerg, "Small-signal stability analysis of inverter-fed power systems using component connection method," *IEEE Trans. Smart Grid*, vol. 9, no. 5, pp. 5301–5310, Sep. 2018.

[11] W. Zhou, R. E. Torres-Olguin, Y. Wang, and Z. Chen, "A gray-box hierarchical oscillatory instability source identification method of multiple-inverter-fed power systems," *IEEE J. Emerg. Sel. Topics Power Electron.*, vol. 9, no. 3, pp. 3095–3113, Jun. 2021.

[12] Z. Yao, P. Therond, and B. Davat, "Stability analysis of power systems by the generalised Nyquist criterion," in *Proc. 1994 Int. Conf. Control*, 1994, pp. 739–744.

[13] X. Wang, F. Blaabjerg, and W. Wu, "Modeling and analysis of harmonic stability in an AC power-electronics-based power system," *IEEE Trans. Power Electron.*, vol. 29, no. 12, pp. 6421–6432, Dec. 2014.

[14] W. Cao, Y. Ma, L. Yang, F. Wang, and L. M. Tolbert, "D–Q impedance based stability analysis and parameter design of three-phase inverter-based AC power systems," *IEEE Trans. Ind. Electron.*, vol. 64, no. 7, pp. 6017–6028, Jul. 2017.

[15] M. K. Bakhshizadeh et al., "The application of vector fitting to eigenvalue-based harmonic stability analysis," *IEEE J. Emerg. Sel. Topics Power Electron.*, vol. 5, no. 4, pp. 1487–1498, Dec. 2017.

[16] M. K. Bakhshizadeh, F. Blaabjerg, J. Hjerrild, L. Kocewiak, and C. L. Bak, "Improving the impedance based stability criterion by using the vector fitting method," *IEEE Trans. Energy Convers.*, vol. 33, no. 4, pp. 1739–1747, Dec. 2018.

[17] B. Gustavsen and A. Semlyen, "Rational approximation of frequency domain responses by vector fitting," *IEEE Trans. Power Del.*, vol. 14, no. 3, pp. 1052–1061, Jul. 1999.

[18] B. Gustavsen, "Improving the pole relocating properties of vector fitting," *IEEE Trans. Power Del.*, vol. 21, no. 3, pp. 1587–1592, Jul. 2006.

[19] A. Rygg and M. Molinas, "Apparent impedance analysis: A small-signal method for stability analysis of power electronic-based systems," *IEEE J. Emerg. Sel. Topics Power Electron.*, vol. 5, no. 4, pp. 1474–1486, Dec. 2017.

[20] J. Beerten, S. D'Arco, and J. A. Suul, "Identification and small-signal analysis of interaction modes in VSC MTDC systems," *IEEE Trans. Power Del.*, vol. 31, no. 2, pp. 888–897, Apr. 2016.

[21] J. Beerten, S. D'Arco, and J. A. Suul, "Frequency-dependent cable modelling for small-signal stability analysis of VSC-HVDC systems," *IET Gener. Transmiss. Distrib.*, vol. 10, no. 6, pp. 1370–1381, Apr. 2016.

[22] Q. Hao, Z. Li, F. Gao, and J. Zhang, "Reduced-order small-signal models of modular multilevel converter (MMC) and MMC-based HVdc grid," *IEEE Trans. Ind. Electron.*, vol. 66, no. 3, pp. 2257–2268, Mar. 2019.

[23] S. D'Arco, J. A. Suul, and J. Beerten, "Configuration and model order selection of frequency-dependent π-models for representing DC-cables in small-signal eigenvalue analysis of HVDC transmission systems," *IEEE J. Emerg. Sel. Topics Power Electron.*, vol. 9, no. 2, pp. 2410–2426, Apr. 2021.

[24] Y. Gu, N. Bottrell, and T. C. Green, "Reduced-order models for representing converters in power system studies," *IEEE Trans. Power Electron.*, vol. 33, no. 4, pp. 3644–3654, Apr. 2018.

[25] M. Rasheduzzaman, J. A. Mueller, and J. W. Kimball, "Reduced-order small-signal model of microgrid systems," *IEEE Trans. Sustain. Energy*, vol. 6, no. 4, pp. 1292–1305, Oct. 2015.

[26] Y. Hu, W. Wu, and B. Zhang, "A fast method to identify the order of frequency-dependent network equivalents," *IEEE Trans. Power Syst.*, vol. 31, no. 1, pp. 54–62, Jan. 2016.

[27] Y. Gu, Y. Li, Y. Zhu, and T. Green, "Impedance-based whole-system modeling for a composite grid via embedding of frame dynamics," *IEEE Trans. Power Syst.*, vol. 36, no. 1, pp. 336–345, Jan. 2021.

[28] W. Zhou, R. E. Torres-Olguin, Y. Wang, and Z. Chen, "DQ impedance-decoupled network model-based stability analysis of offshore wind power plant under weak grid conditions," *IET Power Electron.*, vol. 13, no. 13, pp. 2715–2729, Oct. 2020.

[29] W. Zhou, Y. Wang, and Z. Chen, "Vector fitting-based reduced order modelling method for power cables," in *Proc. IET 15th Int. Conf. AC DC Power Transmiss.*, 2019, pp. 1–6.

[30] W. Zhou et al., "A robust circuit and controller parameters' identification method of grid-connected voltage-source converters using vector fitting algorithm," *IEEE J. Emerg. Sel. Topics Power Electron.*, vol. 10, no. 3, pp. 2748–2763, Jun. 2022.

WEIHUA ZHOU (Member, IEEE) received the B.Eng. and M.Sc. degrees from the School of Automation, Northwestern Polytechnical University, Xi'an, China, in 2014 and 2017, respectively, and the Ph.D. degree from the Department of Energy Technology, Aalborg University, Aalborg, Denmark, in 2020, all in electrical engineering.

He is currently a Research Fellow with the Department of Electrical and Computer Systems Engineering, Monash University, Melbourne, Australia. From 2015 to 2016, he was a Junior Research Assistant with the Department of Mechanical and Automation Engineering, The Chinese University of Hong Kong, Hong Kong. From 2020 to 2020, he was a Visiting Scholar with the Department of Marine Technology, Norwegian University of Science and Technology, Trondheim, Norway. In 2021, He was a Researcher Fellow with the ELECTA Research Group, Department of Electrical Engineering, KU Leuven, Leuven, Belgium, and also with EnergyVille, Genk, Belgium. His research interests include modeling, stability analysis, and control of inverter-based resources.

JEF BEERTEN (Senior Member, IEEE) received the M.Sc. and Ph.D. degrees from the University of Leuven (KU Leuven), Leuven, Belgium, in 2008 and 2013, respectively, both in electrical engineering.

He is currently an Associate Professor with KU Leuven and EnergyVille. In 2011, he was a Visiting Researcher with the Royal Institute of Technology, Stockholm, Sweden, for three months. From 2014 to 2015, he was a Visiting Postdoctoral Researcher with the Norwegian University of Science and Technology, Trondheim, Norway. His research interests include future power system dynamics, modeling, and control.

Dr. Beerten was the first winner of the ABB Research Award in Honor of Hubertus von Gruenberg in 2016 and was the recipient of the KBVE/SRBE Robert Sinave Award and the Prix Paul Caseau from the Institut de France-EDF Foundation for his Ph.D. thesis on modeling and control of dc grids. He is an Active Member of both the IEEE and CIGRE.